

RESEARCH ARTICLE

10.1002/2014JA020695

Key Points:

- Detailed description of the model and comparison case with GEANT4
- The magnetic mirroring ratio is 22% for electrons and 19% for positrons
- Electron beams possibly 50 to 100% larger than previously expected

Correspondence to:

D. Sarria,
david.sarria@irap.omp.eu

Citation:

Sarria, D., P.-L. Blelly, and F. Forme (2015), MC-PEPTITA: A Monte Carlo model for Photon, Electron and Positron Tracking In Terrestrial Atmosphere—Application for a terrestrial gamma ray flash, *J. Geophys. Res. Space Physics*, 120, 3970–3986, doi:10.1002/2014JA020695.

Received 6 OCT 2014

Accepted 13 MAR 2015

Accepted article online 17 MAR 2015

Published online 22 MAY 2015

MC-PEPTITA: A Monte Carlo model for Photon, Electron and Positron Tracking In Terrestrial Atmosphere—Application for a terrestrial gamma ray flash

D. Sarria^{1,2}, P.-L. Blelly^{1,2}, and F. Forme^{1,2}
¹ Université de Toulouse, UPS-OMP, IRAP, Toulouse, France, ² CNRS, IRAP, BP 44346, F-31028, Toulouse, France

Abstract Terrestrial gamma ray flashes are natural bursts of X and gamma rays, correlated to thunderstorms, that are likely to be produced at an altitude of about 10 to 20 km. After the emission, the flux of gamma rays is filtered and altered by the atmosphere and a small part of it may be detected by a satellite on low Earth orbit (RHESSI or Fermi, for example). Thus, only a residual part of the initial burst can be measured and most of the flux is made of scattered primary photons and of secondary emitted electrons, positrons, and photons. Trying to get information on the initial flux from the measurement is a very complex inverse problem, which can only be tackled by the use of a numerical model solving the transport of these high-energy particles. For this purpose, we developed a numerical Monte Carlo model which solves the transport in the atmosphere of both relativistic electrons/positrons and X/gamma rays. It makes it possible to track the photons, electrons, and positrons in the whole Earth environment (considering the atmosphere and the magnetic field) to get information on what affects the transport of the particles from the source region to the altitude of the satellite. We first present the MC-PEPTITA model, and then we validate it by comparison with a benchmark GEANT4 simulation with similar settings. Then, we show the results of a simulation close to Fermi event number 091214 in order to discuss some important properties of the photons and electrons/positrons that are reaching satellite altitude.

1. Introduction

The discovery of terrestrial gamma ray flashes (TGFs) was presented in *Fishman et al.* [1994], using data from the Burst and Transient Source Experiment (BATSE) on board the NASA's Compton Gamma Ray Observatory (CGRO) spacecraft. TGFs are natural bursts of X and gamma rays associated to lightning and detected mostly from space. Later, TGFs have been detected from space by Reuven Ramaty High Energy Solar Spectroscopic Imager (RHESSI) [Smith et al., 2005], Fermi [Briggs et al., 2010], and the Astro-rivelatore Gamma a Immagini Leggero (AGILE) [Marisaldi et al., 2010]. Some attempts have been made to detect TGFs from ground and plane altitude, and Smith et al. [2011] reported the detection of one TGF from the Airborne Detector for Energetic Lightning Emissions (ADELE) instrument. Together with transient luminous events (TLEs), for the optical part, these are short-duration events that play an important role for understanding the magnetosphere-ionosphere-atmosphere coupling [Dwyer et al., 2012; Surkov and Hayakawa, 2012]. This instrumentation helped for important discoveries about TGFs, some of the most important being the following: a photon spectrum coming from an initial Bremsstrahlung spectrum (see below) that is altered while propagating in the atmosphere, a duration typically around 0.4 ms [Briggs et al., 2013] and the constraints on emission altitude that should be between 10 and 20 km, and gamma ray beams with half-angles $>30^\circ$ [Dwyer and Smith, 2005; Carlson et al., 2007; Hazelton et al., 2009; Gjesteland et al., 2011]. The AGILE spacecraft measured a surprising cumulative TGF spectrum with a tail of up to 100 MeV [Marisaldi et al., 2011]. The low-energy part is in good agreement with the standard relativistic runaway electron avalanches (RREA) TGF energy spectrum theory, but the slope at higher energies disagrees with it and may be explained by nonequilibrium acceleration of electrons in lightning [Celestin et al., 2012]. Data from space instrumentation dedicated to the study of TGFs and TLEs, like the Atmosphere-Space Interactions Monitor (ASIM) [Neubert and ASIM Instrument Team, 2009] or the Tool for the Analysis of RAdiation from lightNIing and Sprites (TARANIS) [Lefeuvre et al., 2009], will be available in the next years.

Most of the TGFs are likely to be due to a complex mechanism, involving the acceleration of seed electrons due to electric fields produced in a positive intracloud (+IC) lightning that will produce relativistic

runaway electron avalanches (RREAs) [Gurevich *et al.*, 1992; Babich *et al.*, 2001; Williams, 2010; Williams *et al.*, 2006; Carlson *et al.*, 2010; Celestin *et al.*, 2012]. The RREAs may also be able to seed themselves by the relativistic feedback process [Dwyer, 2012; Liu and Dwyer, 2013]. TGF seeding is discussed in Carlson *et al.* [2008] and Dwyer [2008], among others. The TGF photons due to RREA are produced inside and/or immediately above thunderclouds, by Bremsstrahlung interactions of electrons and positrons with air molecules, with a typical spectrum (photons per unit energy) following $\sim 1/E$ with an exponential cutoff. The electrons and positrons responsible for the Bremsstrahlung photon emission are not escaping to space because they lose all their energy by undergoing a large amount of collisions with air molecules and therefore cannot leave the region of production. Electrons do not escape to satellite altitude if they do not reach at least ~ 35 km altitude.

Once produced, these primary Bremsstrahlung photons interact with the atmosphere while propagating. Few percent of them will escape, if they reach an altitude above ~ 100 km (where the mean free path goes above 1000 km). The result of their interactions are secondary electrons and positrons (which are referred to as “leptons” hereafter) that will be confined by the magnetic field of the Earth, forming the so-called terrestrial electron beams (TEBs). The secondary electrons are due to Compton scattering, photoionization, and pair production, while positrons are only produced by electron/positron pair production. The leptons may add even more electrons to the system by inelastic scattering or more photons by Bremsstrahlung. These leptons may reach an altitude where their mean free path allows them to escape; in that case their motion is controlled by the geomagnetic field and thus they may bounce on magnetic mirror points, leaving a specific signature of a dual pulse in satellite measurements, as shown, for example, by Fermi in Briggs *et al.* [2010]. Prior to Fermi, TEBs have also been detected by CGRO/BATSE [Dwyer, 2008] and RHESSI [Smith *et al.*, 2006], and some candidates were found using the Solar Anomalous and Magnetospheric Particle Explorer data Carlson *et al.* [2009]. These observations show that TEBs have significantly longer time scales than TGFs, and their detected energy spectra seems to present a clear bump around 511 keV (a signature of positron annihilation).

The problem of TGF’s particles propagation in Earth’s Atmosphere has already been assessed by several other authors. Østgaard *et al.* [2008] presents a Monte Carlo model that can simulate TGFs’ propagation in the atmosphere, which is focused on giving the properties of the escaping photons and is then used to give constraints on the TGF source properties, consistently with the standard picture. It cannot give full information about the electrons reaching satellite altitude: the electrons are created by photon interactions but not transported then. The Bremsstrahlung is simulated through a continuous energy loss formula from the properties of the produced electron. It was used to give good constraints on the TGF source altitude as well as emission angle.

In Carlson *et al.* [2011], simulations using the GEometry AND Tracking version 4 (GEANT4) toolkit are used below 150 km altitude, coupled with a guiding center solver for electron motion for higher altitudes. The main results of this study were to give the electrons fluences (particules/cm²) for different source configurations and to show that these secondary electron beams may be too faint to be detected from satellites as often as photons.

The REAM model (Runaway Electron Avalanche Model) is used in Dwyer *et al.* [2008] to simulate TGF and associated TEBs. This Monte Carlo model is able to follow photons and electrons with all the relevant processes and is presented in detail in Dwyer and Smith [2005] and Dwyer [2007]. In Dwyer *et al.* [2008], it is estimated that TEBs will be detected about 100 times less than TGFs by satellites at ~ 600 km altitude. Because the electron beams are confined by the geomagnetic field, their fluence is actually higher at this altitude. Indeed, the electron fluence remains roughly constant during the propagation, whereas the fluence of photons will fall off as $1/r^2$. The production of electrons that can reach satellite altitude is considered to start at around 30–40 km and to be mainly produced within an atmospheric scale height (of about 7 km), giving electron beam sizes of ~ 10 km radius.

In this article, we present a new Monte Carlo model called MC-PEPTITA, for “Monte Carlo Photon, Electron and Positron Tracking In Terrestrial Atmosphere,” which has been developed to give a comprehensive view of the dynamics of leptons and photons. It is able to track photons, electrons, and positrons that propagate in the Earth space environment, atmosphere, and geomagnetic field. All the secondary, tertiary, and further particle production are accounted for. The full information of each particle reaching satellite altitude, as well as information about their production conditions, are saved.

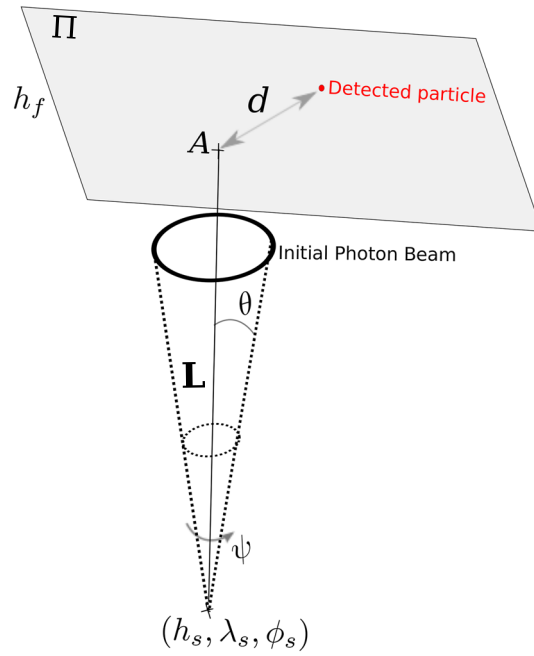


Figure 1. (h_s, λ_s, ϕ_s) : coordinates of the point source of initial photons. \mathbf{L} : local vertical unit vector based on (h_s, λ_s, ϕ_s) . θ : opening angle of the photon beam. ψ : azimuthal angle of the photon beam. Π : part of the detection sphere where the detected particles are spread. A : intersection between Π and \mathbf{L} . d : radial distance between point A and a detected particle.

source located at coordinates (h_s, λ_s, ϕ_s) (see Figure 1 for the geometry of the emission). In Figure 1 we show the geometry of this point source. The parameters describing the source geometry are

1. \mathbf{L} : the local vertical direction.
2. θ : opening angle of a sampled photon.
3. ψ : azimuthal angle of a sampled photon.
4. d : radial distance of a detected particle.

The source is considered to be oriented toward the zenith. The detailed calculation of the radial distance d is presented in Appendix A. In all the simulations presented in this paper, ψ is uniformly sampled between 0 and 2π radians. As argued in Carlson *et al.* [2011], θ is sampled with a probability density function (PDF) given by

$$P_\theta(\theta) = A \exp\left(\frac{-\theta^2}{2\sigma_\theta^2}\right) \quad (1)$$

A is a normalization factor; σ_θ measures the width of the beam and ranges from 5° to 60° .

2.2. Initial Energies

Let E be the energy of a primary photon. A TGF Bremsstrahlung spectrum has a probability density function that can be approximated with [Dwyer *et al.*, 2012]:

$$P_E(E) = \frac{E_0}{E} \exp\left(\frac{-E}{\epsilon}\right) \quad (2)$$

Where E_0 is a normalization factor. The cutoff energy ϵ has a typical value of 7.3 MeV. This value is known to give a spectrum reasonably close to the exact spectrum [Dwyer *et al.*, 2012; Coleman and Dwyer, 2006]. Let E_{\min} be a threshold energy and E_{\max} be a maximum energy; reasonable values are 10 keV and 30 MeV, respectively.

MC-PEPTITA model is presented in section 2, in particular the initial conditions, the relevant parameters, and the methods used for transportation of photons, electrons, and positrons. At the end of this section we compare MC-PEPTITA model with a GEANT4 similar setup. In section 3, MC-PEPTITA is used to study some features of the particles propagating the atmosphere, especially in the frame of the Fermi event number 091214 observations [Briggs *et al.*, 2011].

2. Model Presentation

MC-PEPTITA is a three-dimensional code for positions and velocities of the particles. We use the Earth-Centered Earth Fixed referential. A simulation starts with N primary photons, with spatial, energetic, and temporal properties discussed hereafter. As soon as they are created, the particles are propagated in Earth's atmosphere and magnetic field until they disappear (because its energy goes below the threshold or the interaction itself removes the particle) or reach a limit altitude (of a satellite, for example); leptons are not removed if they reach the limit altitude, but the number of times they have crossed the surface at that altitude is saved.

2.1. Initial and Final Geometric Parameters

The initial TGF photons are generated from a point

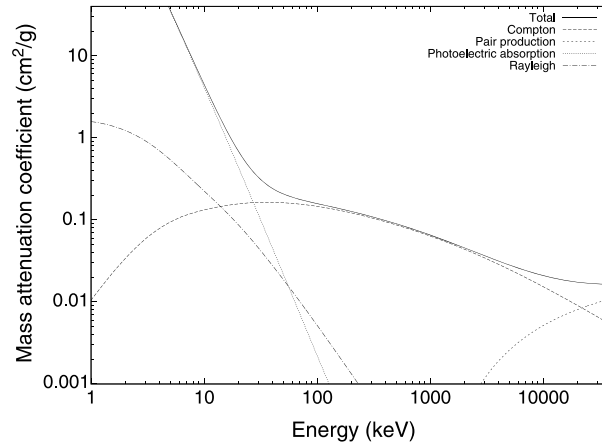


Figure 2. Photon mass attenuation coefficients in air, versus energy, for the four considered processes. The energy ranges from 1 keV to 40 MeV. O₂ and N₂ are considered, with densities calculated with NRLMSISE-00.

It has been estimated that, in a real TGF, at least 10^{16} primary photons can be emitted [Dwyer, 2012] for an emission altitude of 15 km. Recently, Cummer *et al.* [2014] could estimate, for two TGF events, a production altitude ranging from about 11 to 13 km, with an intrinsic brightness of 10^{18} electrons. These electrons could produce about 10^{17} TGF photons [Dwyer *et al.*, 2012]. For computational reasons, we cannot initiate simulations with so much photons, and therefore a proper scale factor has to be applied for output quantities that depends on photon number if one wants to interpret it as realistic values.

2.3. Photon, Electron, and Positron Path

While propagating in the atmosphere, the photons can interact with air molecules (O₂ and N₂) and can undergo Compton scattering, photoelectric absorption, electron/positron pair production, and Rayleigh scattering. The produced

electrons can undergo inelastic scattering, elastic scattering, and Bremsstrahlung. The produced positrons can undergo the same interactions as electrons and can also annihilate into two photons.

2.3.1. Path Length and Attenuation Coefficients

Let the path length $s > 0$ be the distance between two interactions. The probability that an interaction takes place before reaching the distance s is given by [Kalos, 1986]

$$U(s) = 1 - \exp \left[- \int_0^s \iota(s') ds' \right] \quad (3)$$

where $L_{i_{\text{par}}} = 1/\iota$ is the mean free path of a particle which travels a distance s . For a photon or a lepton, $\iota(s) = \mu_{\text{att},i_{\text{par}}} \rho(h)$. Where $\rho(h)$ is the atmosphere mass density at the altitude h , $\mu_{\text{att},i_{\text{par}}}$ is the total attenuation coefficient for a given particle, and i_{par} indicates the particle type (photon, electron, or positron). The $\mu_{\text{att},i_{\text{par}}}$

will have a different value for photons, electrons, and positrons and will also vary with the altitude and the energy of the particle. It is given by

$$\mu_{\text{att},i_{\text{par}}}(E, h) = N_a \sum_{i_{\text{proc}}=1}^{n_{\text{pc}}} \sum_{i_{\text{sp}}=1}^{n_{\text{sp}}} \frac{e_{i_{\text{sp}}}(h)}{A_{i_{\text{sp}}}} \sigma_{i_{\text{proc}},i_{\text{sp}}}^{i_{\text{par}}}(E) \quad (4)$$

where n_{pc} is the total number of processes and depends on i_{par} , n_{sp} is the total number of neutral species, i_{proc} is the process index, i_{sp} is the species index, N_a is the Avogadro number, $A_{i_{\text{sp}}}$ is the molar mass, and $e_{i_{\text{sp}}}$ is the density proportion. The atmospheric density profile is approximated by $\rho(h) = \rho_0 e^{-ah}$, where a is the inverse of the atmospheric scale height and ρ_0 a reference density. The values of a and ρ_0 can be derived at any step by computing and fitting the corresponding NRLMSISE-00 density profile

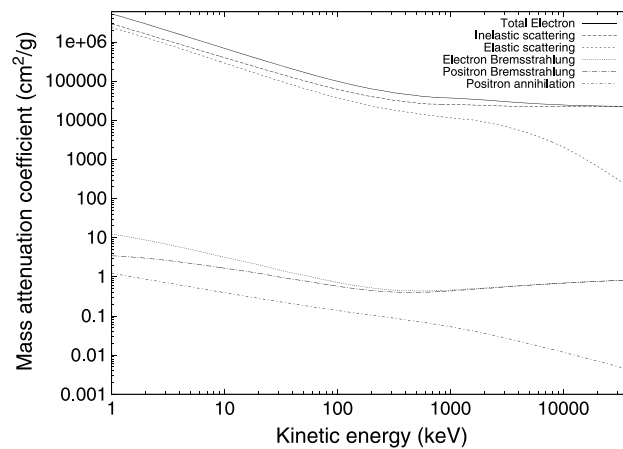


Figure 3. Electron and positron mass attenuation coefficients in air, versus kinetic energy, for the considered processes. The energy ranges from 1 keV to 40 MeV. O₂ and N₂ are considered, with densities calculated with NRLMSISE-00. The difference of attenuation coefficients for elastic and inelastic scatterings is indistinguishable between electron and positron, in the scale of this plot. The annihilation is only possible for positrons. Positron and electron Bremsstrahlung is distinguishable in the scale of this figure for energies below ~ 600 keV.

[Picone *et al.*, 2002]. The value of $1/a$ is typically about 7 km. To gain computing time, it is interesting to call NRLMSISE-00 only once per step. We can then locally use the approximation that $a = Mg/RT$, where R is the gas constant, M is the molar mass of the air, and g is the Earth's gravitational acceleration. To gain even more computing time, a constant value of a and ρ_0 may be used for the whole simulation while introducing a higher error than the previous method.

The atmosphere is composed of O_2 and N_2 . In Figures 2 and 3 we show the mass attenuation coefficients in the air of photons and leptons for the different processes, as a function of the energy. Their relative importance is discussed in detail in section 2.4.

2.3.2. Photon Transport and Electron/Positron Transport With Constant Magnetic Field

To sample the path length s of a particle between two interactions, we use a formula similar to equation (A4) of Østgaard *et al.* [2008], based on a quasi-exponential atmosphere approximation, and derived from equation (3). At 15 km altitude, for 10 keV particles, the path length is typically around 2 km for photons and 2 cm for electron/positrons. It increases quasi-exponentially with altitude, following the atmospheric density decrease, with a scale height of around 7 km. The path length also increases with energy, as the total attenuation coefficient decreases with energy (see Figures 2 and 3).

For photons, the trajectories between two interactions are straight lines. The orientation of a photon can change only because of Rayleigh and Compton scattering. Updating the position of a particle is done with

$$\mathbf{r}_1 = \mathbf{r}_0 + s \hat{\mathbf{v}} \quad (5)$$

where \mathbf{r}_0 is the initial position vector of the particle, \mathbf{r}_1 is the position of the particle after traveling the path length s , $\hat{\mathbf{v}} = \mathbf{v}/v$ is the normalized velocity, and v is the speed of the particle.

For charged particle, the effect of the deviation due to the magnetic field is nonnegligible above ~60–70 km. The magnetic field can be considered roughly constant between two collisions at altitudes lower than 90 km, since the path length for electrons will be below 1 km. Updating the velocity of the leptons is done with

$$\mathbf{v} = \mathbf{v}_0 + (\cos(\theta) - 1) \mathbf{v}_{0\perp} + \sin(\theta) \mathbf{v}_{0\parallel} \quad (6)$$

where \mathbf{v}_0 is the initial velocity of the particle and $(\mathbf{v}_{0\parallel}, \mathbf{v}_{0\perp})$ the components of the initial velocity vector that are parallel and perpendicular to the magnetic field. The angle $\theta = s \frac{eB}{\gamma m v_0}$, where e is the (positive) elementary charge, m is the mass of the electron, B is the magnitude of the magnetic field, and v_0 is the magnitude of \mathbf{v}_0 .

2.3.3. Electron/Positron Transport With Varying Magnetic Field

In MC-PEPTITA, the geomagnetic field is provided by the IGRF-11 model [Finlay *et al.*, 2010]. The motion of the e^-/e^+ in the geomagnetic field follows the basic equations of charged particle motion in a magnetic field that we normalized for our problem:

$$\frac{d\beta}{ds_n} = -\frac{Z_0}{\gamma} \frac{\beta}{\beta} \times \mathbf{B}_n \quad (7)$$

$$\frac{d\mathbf{r}_n}{ds_n} = \frac{\beta}{\beta} \quad (8)$$

with $\mathbf{B}_n = \mathbf{B}/B_e$, $s_n = s/\frac{c}{\Omega_0}$, $\mathbf{r}_n = \mathbf{r}/\frac{c}{\Omega_0}$, and $\beta = \mathbf{v}/c$. $\Omega_0 = eB_e/m$, where Z_0 is -1 for electrons and $+1$ for positrons, c is the speed of light in vacuum, and B_e is the geomagnetic field magnitude at the magnetic equator. This differential equation system is solved using a fourth-order Runge-Kutta solver.

2.3.4. Intermediate Regime

The Runge-Kutta method will require a step δs . It is chosen to be small enough (at least 10 times less) compared to the mean free path or the Larmor radius (the smallest of the two is considered). In this case, the Runge-Kutta method is used as well, but each step is checked for an interaction. The following algorithm is applied:

1. Random sample a number ξ uniformly distributed between 0 and 1.
2. For each Runge-Kutta step, the sum $S_n = \sum_{i=1}^n t_i \delta s$ is incremented, and $U_n = 1 - \exp(-S_n)$ is evaluated, where n is the number of the current step and $1/t_i$ is the local mean free path during the step number i . It corresponds to a discretized form of equation (3).

Table 1. Summary of the Processes and Total Cross Sections Used in MC-PEPTITA

Particle	Processes	Total Cross-Section Source
Photon	Compton acattering Photoelectric absorption Rayleigh scattering e ⁻ /e ⁺ pair production	EPDL ^a
Electron	Inelastic scattering Bremsstrahlung Elastic scattering	EEDL ^b Seltzer-Berger ^c EEDL ^b
Positron	Inelastic scattering Bremsstrahlung Elastic scattering Annihilation	EEDL ^b Seltzer-Berger ^c with analytical correction ^d ELSEPA ^d and EEDL ^b Analytical formula ^d

^aCullen *et al.* [1997].^bPerkins *et al.* [1991].^cSeltzer and Berger [1986].^dSalvat *et al.* [2011].

3. At each Runge-Kutta step, the condition $U_n > \xi$ is checked. If it is true, an interaction of the electron/positron takes place.

In principle, this method could be used at any altitude. Nevertheless, it will require very low Runge-Kutta steps at low altitude (< 30–40 km) that will involve very long computation times. The criteria of transition between this regime and the two others is discussed next.

2.3.5. Criteria to Choose Between the Three Descriptions of Electron/Positron Transport

Let us define two frequency scales:

1. The mean collision frequency: $f_c = \frac{v_{\parallel}}{L_{i\text{par}}}$
2. The gyration frequency: $f_g = \frac{1}{2\pi} \frac{eB}{m\gamma}$

where v_{\parallel} is the magnitude of the velocity parallel to the geomagnetic field. The f_c decreases exponentially with increasing altitude (since the mean free path $L_{i\text{par}}$ increases) and f_g also decreases but much more slowly. When $f_c > 100f_g$, the transport of e⁻/e⁺ is made according to the method of section 2.3.2, and if $f_g > 100f_c$ the transport of e⁻/e⁺ is made according to section 2.3.3. If the frequencies are not included in one range or the other, the intermediate method is used (section 2.3.4).

2.3.6. Alternative Method

The method presented in the previous section can be simplified in order to reduce substantially the computation time. The simpler method consists in not using the intermediate regime and instead to use a sharp transition between the collisional regime (section 2.3.2) and the fully magnetized regime (section 2.3.3) by just checking if $f_c > f_g$ or not. The results obtained using this faster method are very similar, at least for the simulations presented in this work. Nevertheless, this may not be verified in the general case and one should be careful when using this alternative method.

2.4. Interaction Processes

The cross-section sets of the Evaluated Photon Data Library (EPDL) and the Evaluated Electron Data Library (EEDL) [Perkins *et al.*, 1991; Cullen *et al.*, 1997] (from Lawrence Livermore National Laboratory) are mainly used. The EPDL and EEDL tabulated cross sections' energies range from 10 eV to 1 GeV. For elastic scattering of positrons, we use data from the "Dirac partial-wave calculation of ELastic Scattering of Electrons and Positrons by Atoms, positive ions and molecules" (ELSEPA) database for energy range < 500 keV [Salvat *et al.*, 2005]. The inelastic scattering cross section is given by the sum of electron ionization and excitation cross sections given in EEDL. We suppose that electrons and positrons have similar inelastic scattering cross sections in the considered energy range (1 keV to 40 MeV). The Bremsstrahlung cross sections are taken from Seltzer and Berger [1986], taking into account electron-nucleus and electron-electron Bremsstrahlung. We also use analytic formulas for positron annihilation and to correct the Bremsstrahlung cross section for positrons [Salvat *et al.*, 2011]. Table 1 summarizes all the involved particles and processes, the total cross sections used for each, and the references.

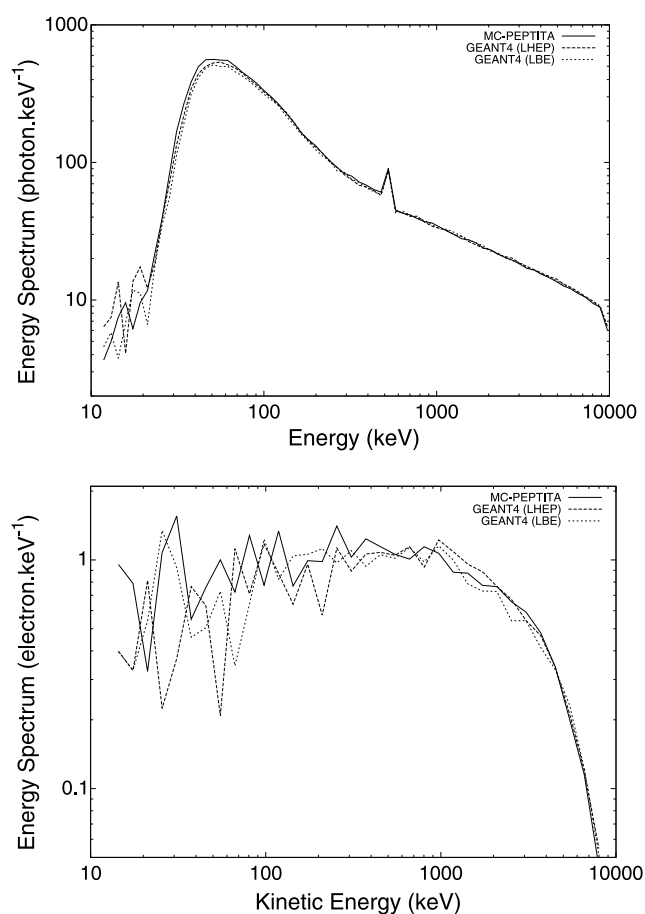


Figure 4. (top) Energy spectrum of photons detected at 100 km altitude from an initial source of photons located at 15 km altitude, detection at 100 km altitude, and more details presented in section 2.6. We compare MC-PEPTITA with a GEANT4 simulations (two physics lists). (bottom) Similar to Figure 4 (top) but for electrons.

The mass attenuation coefficients are calculated from the cross sections and the atmospheric densities, as presented in equation (4). In Figures 2 and 3 we show the mass attenuation coefficients in the air of photons and leptons for the different processes, as function of energy.

For photons, from 10 keV (our threshold energy) to about 30 keV, the interactions are dominated by photoelectric absorption. From about 40 keV to around 10 MeV, Compton scattering dominates. Above several MeV, electron/positron pair production becomes nonnegligible and more and more important with increasing energy and dominates above 25 MeV. All these three processes will be responsible of production of secondary electrons, and pair production will also produce secondary positrons. In both pair production and photoelectric absorption, the photon will be lost. In Compton scattering, both the direction and the energy of the photon are changed. On the other hand, Rayleigh scattering never dominates over other processes. Rayleigh scattering changes the orientation of the photon without changing its energy. Therefore, it is likely to have a negligible impact on the simulation results. In section 3.1 we discuss the proportion of escaping particles with respect to the process responsible for their creation.

In Figure 3, for the electrons, we see that both elastic and inelastic scattering are dominating in the whole considered kinetic energy range. Inelastic scattering is always more dominant than elastic scattering and becomes more dominant for increasing kinetic energy. In the whole energy range, Bremsstrahlung and positron annihilation always remain orders of magnitude less important than the two other processes. Nevertheless, Bremsstrahlung is not negligible in practice, as discussed in section 3.1. It will actually dominate the energy loss of electrons and positrons above 2 MeV [Dwyer *et al.*, 2012], since the energy loss due to inelastic scattering will be an order of magnitude less than the energy loss due to Bremsstrahlung. For the positrons, the fact that the annihilation cross section never dominates in the whole energy range

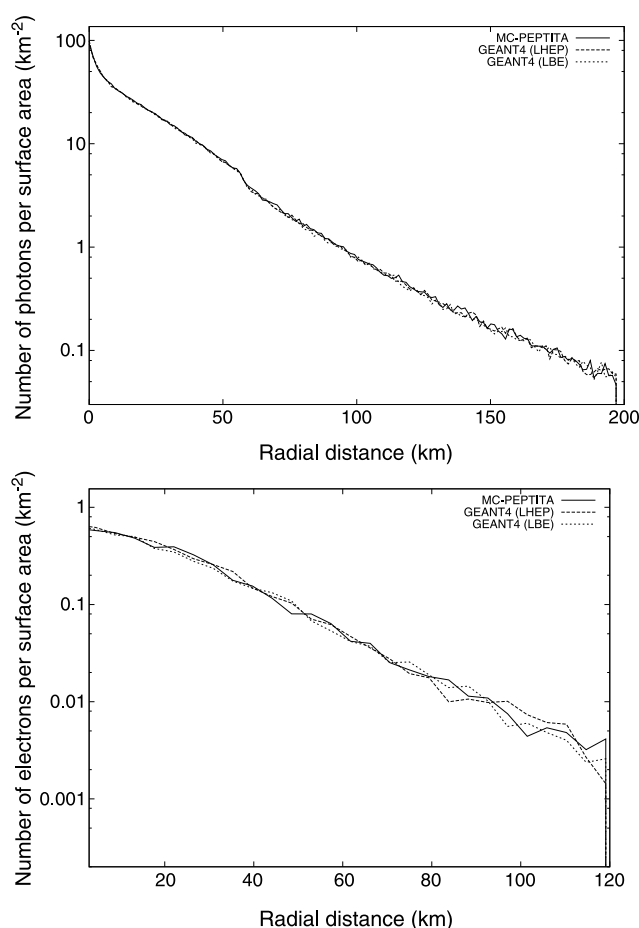


Figure 5. (top) Radial distance distribution of photons detected at 100 km altitude from an initial source of 10^7 photons located at 15 km altitude, detection at 100 km altitude, and further details presented in section 2.6. We compare MC-PEPTITA with GEANT4 (two physics lists). (bottom) Similar to Figure 5 (top) but for electrons.

only means that in-flight annihilation will be very unlikely. Actually, the positrons will lose almost all their kinetic energy with inelastic scattering and will only be able to elastic scatter or annihilate and therefore will eventually annihilate with almost no kinetic energy. The rest of the energy of electrons and positrons is close to 511 keV, and in the annihilation process a positron and an electron will annihilate, leaving two photons with energies close to 511 keV. In our simulations, we annihilate positrons when their energy goes below the threshold energy of E_{\min} . Therefore, the spatial and time information about the resulting annihilation photons may have some uncertainties (but time domain is not discussed in this article). These annihilation photons are very concentrated around the energy of 511 keV and thus will have a clearly visible effect on the energy spectrum (see Figure 4).

The simulation of the interactions is done (for photons, electrons, and positrons) similarly to what is presented in the Penetration and ENERGY LOSS of Positrons and Electrons (PENELOPE) code [Salvat *et al.*, 2011]. It is important to remark that, compared to some previous works, the Compton scattering is simulated using semianalytic profiles, which change shape when using different atomic numbers.

2.5. Particle Detection

It is necessary to have a criterion to know how a particle is considered as detected in MC-PEPTITA simulations. Any photon that reaches 550 km altitude is saved. Electrons and positrons are recorded if they cross satellite altitude either in upward or in downward direction, and they are propagated until they are absorbed by the atmosphere or if their time value goes above 1 s after their emission time. Therefore, e^+/e^- can be detected twice or more times, as illustrated in Figure 11. This information is stored for each particle.

Table 2. Photon, Electron, and Positron Number Reaching 100 km Altitude for MC-PEPTITA and GEANT4 Simulations (With the LHEP and LBE Physics Lists)^a

Simulation	MC-PEPTITA	GEANT4 (LHEP)	GEANT4 (LBE)
Photon count	218,459	217,658	215,500
Electron count	3,516	3,547	3,369
Positron count	239	237	245
Positron ratio	6.4 %	6.3 %	6.8%

^aThese results are from the benchmark simulation, with a source of 10^7 photons. More details in section 2.6.

All particles with energies below E_{\min} are lost, and positrons going below this threshold will be considered to lose all their energy and annihilate. This threshold is set because

1. Some data of EPDL and EEDL data sets are not recommended to be used below 1 keV.
2. The mean free path of low-energy particles is very low (especially for leptons). Therefore, computation time increases exponentially as we decrease the threshold energy.

3. The outgoing photons have energy that are anyway cut off by the atmosphere for energies below ~ 10 –30 keV (see Figure 4).

In each simulation presented here, more than 10^{10} electrons are produced with energies below E_{\min} . All these particles should be interesting in terms of production of excited states, possible optical emissions, and possible effects on the ionosphere and would deserve further study using a more accurate code for particle transport in the sub-keV energy range.

2.6. MC-PEPTITA and GEANT4 Comparison

In this section, we want to compare the MC-PEPTITA model with the GEANT4 toolkit. GEANT4 is a code developed by an international cooperation led by CERN [Agostinelli et al., 2003]. Its primary use is for high-energy physics simulations involving particle detectors, radiation dosimetry, or predictive modeling. As it is used for detectors, it is made to handle only geometrical elements of constant densities. Therefore, for the GEANT4 benchmark setup, we approximated the atmosphere with 500 exponentially distributed density layers between 0 and 100 km. GEANT4 can run with different physics lists. The most appropriate ones for this problem are the low-energy ones: LHEP and LBE. The LHEP stands for “Low and High Energy Parameterization model.” LBE stands for “Low Background Experiment.” A recent article by [Skeltved et al., 2014] discussed the differences between the use of these two physics lists, in the context of the relativistic feedback TGF production mechanism, and showed some significant differences between them. It is then important to compare it in the context of atmospheric propagation of TGFs as well.

We run simulations with MC-PEPTITA and with GEANT4 (both physics lists) with a common setup, chosen as

1. $E_{\min} = 10$ keV, $E_{\max} = 10$ MeV.
2. 10^7 photons emitted with a $1/E$ power law (no exponential cutoff).
3. Source at 15 km, detection at 100 km.
4. Zenith-oriented initial beam. The polar angle θ is sampled uniformly between 0° and 35° . The azimuthal angle ψ is sampled uniformly between 0° and 360° .
5. Atmosphere with O_2 and N_2 , with proportions and densities calculated with NRLMSISE-00.
6. No magnetic or electric field.

We compare the particle distributions obtained at 100 km with the two models by looking to two quantities: the radial distance distribution and the energy spectrum distribution, both defined in Appendix A. We choose these quantities because they are a good indicator of what we are actually simulating: a degradation of energy and a spatial dispersion of the particles.

The radial distance distribution and the energy spectrum distribution for photons and electrons reaching 100 km altitude are shown in Figures 5 and 4, for GEANT4 (both physics lists) and MC-PEPTITA simulations. For the photon distributions, GEANT4 simulations give very similar results for both physics lists and the relative difference between MC-PEPTITA and GEANT4 is less than 2%, for either radial distance distribution or spectrum. It is essentially because of the following:

1. We use the same atmosphere model to compute the densities of N_2 and O_2 . Nonetheless, in the GEANT4 setup the particles are transported in layers of constant densities and in MC-PEPTITA they are transported in an exponential atmospheric profile.

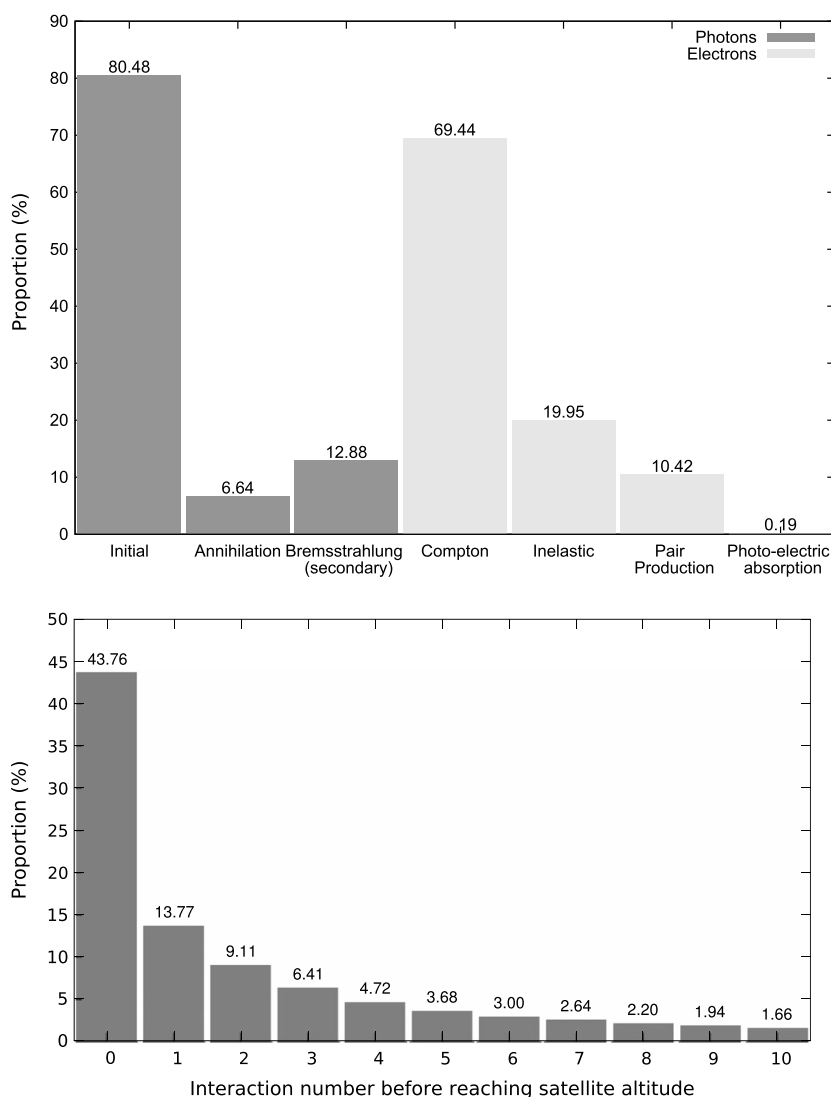


Figure 6. (top) Proportion, over all the particles of the same type (photon or electron), of particles created by all the processes that can create particles: Initial photon, e^-/e^+ annihilation, Bremsstrahlung, Compton scattering, inelastic scattering, e^-/e^+ pair production, and photoelectric absorption. (bottom) Percentage of photons (reaching 550 km altitude) that have undergone a given number of interactions. We show the values from 0 to 10, but photons can do more interactions. For both figures, we consider only particles detected one time.

2. Most of the cross-section sets used are similar, as well as the way we model the interactions.

In the electron distributions, the statistic is smaller; therefore, more noise is present. In the energy spectrum (Figure 4), MC-PEPTITA and GEANT4 are very consistent within the statistical noise. For the radial distance distribution (Figure 5), MC-PEPTITA and GEANT4 simulations are also very consistent, considering the statistical noise. The differences for electrons are attributed to the same reasons as for the photons.

Table 2 presents the photon, electron, and positron number count for the benchmark simulations. We can see that the number of photons, electrons, and positrons reaching 100 km are similar within $\sim 5\%$ for all the simulations. Δ_p is the positron fraction. It can be defined as $N(e^+)/N(e^+ + N(e^-))$. It is about 6.5% for all simulations.

3. Some Properties of TGF Particles Reaching Satellite Altitude

In this section we draw a picture of the TGF particles reaching satellite altitude. We choose to run MC-PEPTITA with a setup close to the Fermi event number 091214 observations, presented in Briggs *et al.* [2011]. The likely

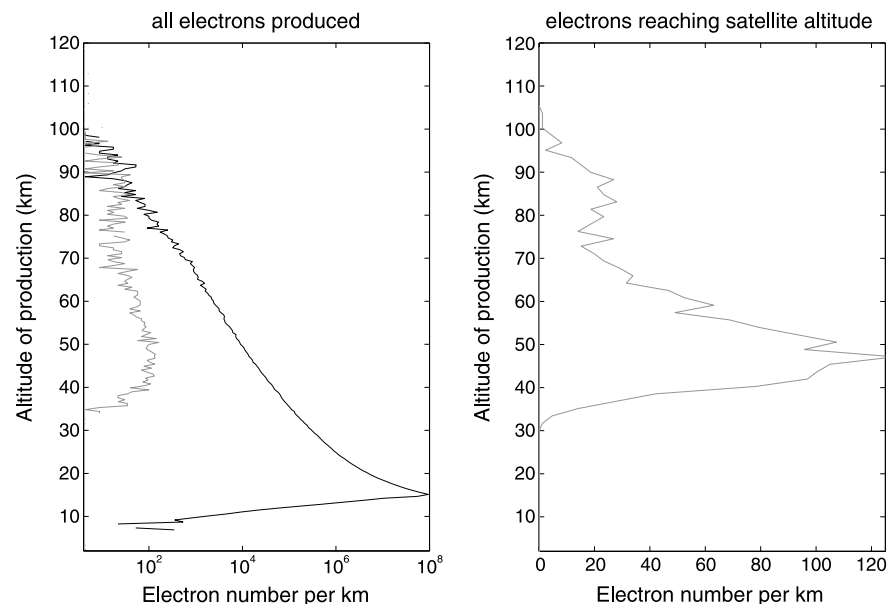


Figure 7. Production rates of electrons (electrons/km) with energies above 10 keV. (left) In log scale, all the production and (right) in linear scale, the production rate of electrons that are going to reach 550 km altitude. Figure 7 (right) is reproduced in log scale inside Figure 7 (left), for comparison. These results come from the simulation described in section 3.

source is situated at 32° longitude and -13° latitude (i.e. in the Southern Hemisphere). The initial setup uses these assumptions:

1. The altitude of the initial TGF source is 15 km. The altitude of detection is set to 550 km.
2. The initial photon beam properties follow what is presented in sections 2.1 and 2.2, with the parameters set to $\sigma_\theta = 35^\circ$ for the opening zenith angle, $E_{\min} = 10$ keV, $E_{\max} = 30$ MeV for the energy range, and $\epsilon = 7.3$ MeV for the exponential cutoff.
3. $N = 2 \times 10^7$ initial photons.

3.1. Production Processes

Figure 6 (top) shows the percentage of outgoing photon produced by the different processes. It corresponds to all the particles but is detected only once. About 80% of the photons reaching the 550 km frontier are from the initial source. Figure 6 (bottom) shows the number of interactions of the outgoing photons. We see that $\sim 75\%$ interacted less than 4 times. Most of these interactions correspond to Compton scattering because the cross section dominates Rayleigh scattering in the whole energy range, and the other possible processes (photoelectric absorption and pair production) lead to removing the photon from the simulation. The photons due to positron annihilation represents $\sim 7\%$. Annihilation photons leave a clearly visible signature around 511 keV in the energy spectrum (see Figure 9), which is the energy of the rest mass of positrons and electrons. The photon part due to secondary Bremsstrahlung represents $\sim 13\%$. Figure 6 (bottom) shows that $\sim 69\%$ of the electrons are due to Compton scattering, $\sim 21\%$ to inelastic scattering, and $\sim 10\%$ to electron/positron pair production. Almost no electron produced by photoelectric absorption reaches 550 km altitude. The electrons due to photoelectric absorption will be produced by the photons with the lowest energies: it will be difficult for them to have enough energy to reach satellite altitude. The origin of the positrons is clear since their production is only possible by electron/positron production of gamma rays interacting with air molecules.

3.2. Production Altitudes of Leptons

In Figure 7, we present the production altitudes of all the secondary electrons. In the same figure, we show the altitudes of production of electrons that have reached satellite altitude, considering only the population detected for the first time, in the Southern Hemisphere (as presented in Figure 11).

As seen in Figure 7 (left), some electrons can be produced below the initial source altitude of 15 km, because some photons can Compton scatter backward and Compton scatter again (or do pair production or photoelectric effect with a lower probability) at a lower altitude. On the same plot, the total electron

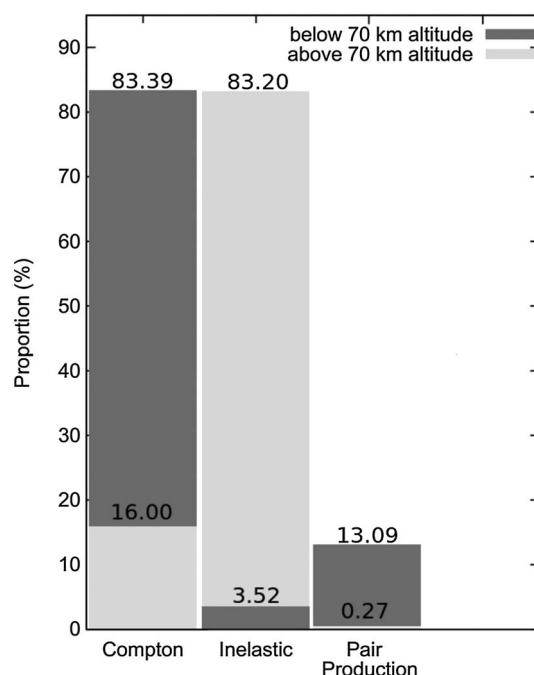


Figure 8. Histogram of the production source for all the electrons reaching 550 km altitude (and detected one time); we discriminate between the ones that have been produced above and below 70 km altitude. Above 70 km altitude, the production of electrons reaching 550 altitude is dominated by inelastic scattering (of electrons), and below 70 km altitude, it is dominated by Compton scattering (of photons) and pair production is important. Photoelectric absorption is negligible.

the escaping electrons produced between 28 and 70 km is ~ 7.4 MeV, and the average energy of escaping electrons produced between 70 and 100 km is ~ 460 keV.

3.3. Energy Spectra

The photon, electron, and positron energy spectra are presented in Figure 9. Consider first the photon spectrum. Below ~ 25 keV, there is a strong decrease due to photoelectric absorption. For higher energies, the

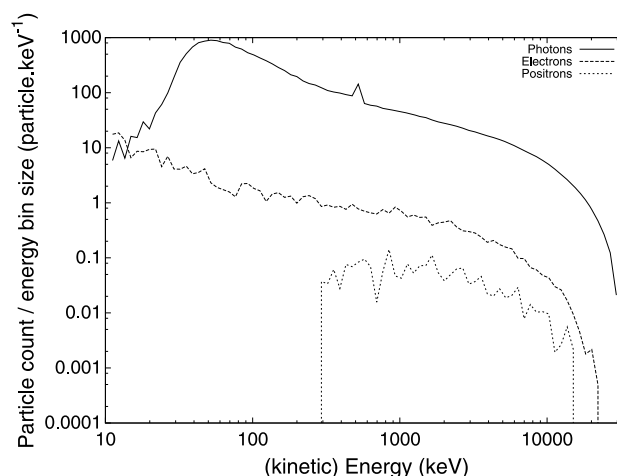


Figure 9. Photon, electron, and positron energy spectra for the simulation described in section 3. We consider only particles detected the first time. There is a scale factor of about 56 between electrons and photons and of about 10 between positrons and electrons. A 511 keV bump is presented, due to annihilation of positrons. The photon and electron energy spectra are in the same order of magnitude for energies below ~ 14 keV.

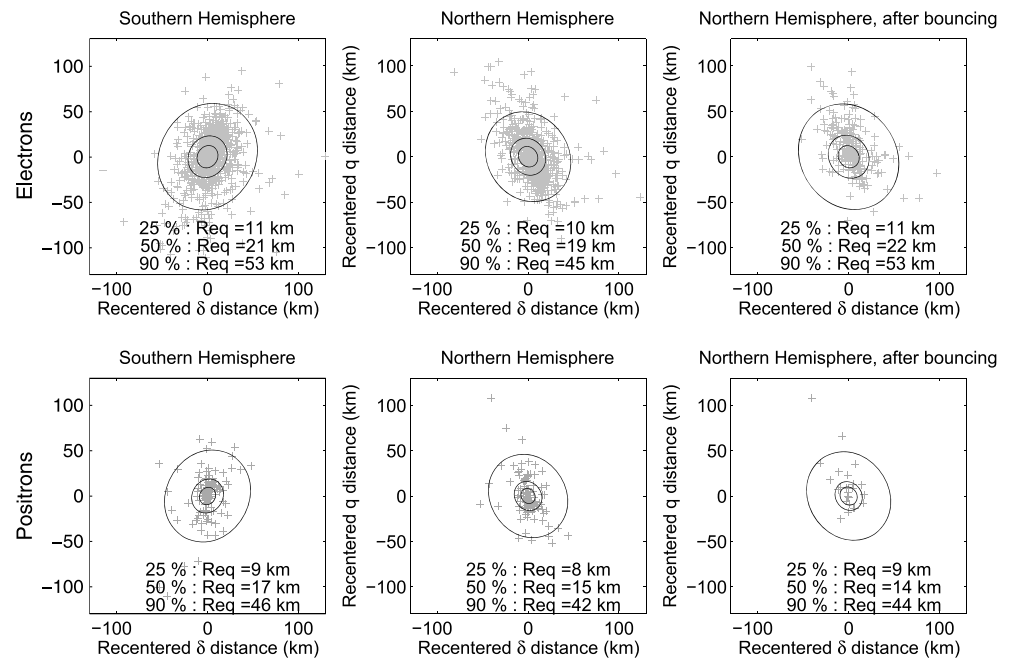


Figure 10. Positions of electrons and positrons crossing satellite altitude in the Northern and Southern Hemispheres (for number of detection ≤ 3). The distances labeled δ and q are calculated from longitude and latitudes (see section A4) and centered each time on the center of the considered beam. The ellipses contain, from smallest to largest, 25%, 50%, and 90% of the particles present in each square, and the equivalent radius of each ellipse (as defined in section 3.4) is given inside of each subplot.

spectrum increases and reaches a maximum at around 50 keV. Then, it decreases following roughly the shape of the Bremsstrahlung spectrum initially emitted. At around 511 keV, there is a small bump due to photons produced by positron annihilation. Note that the initial considered photon spectrum at 15 km has no 511 keV line; this feature is due to annihilation of positrons produced by the primary photon source.

Above 50 keV, the electron spectrum is similar to the photon spectrum but with a scale factor of about 56. Below 50 keV, there is no strong decrease in the electron spectrum, and it follows roughly the shape of the initial photon spectrum. The 511 keV bump is not present. Electron and photon spectra are within the same order of magnitude for energies below ~ 14 keV.

For positrons, the statistics is rather bad. The positron energy spectrum seems quite similar to the high-energy part (1 MeV to 10 MeV) of the electron spectrum. Indeed, positrons can only be produced by pair production, which produces (on average) more energetic leptons than other processes that can produce only electrons (Compton scattering, inelastic scattering, and photoelectric absorption).

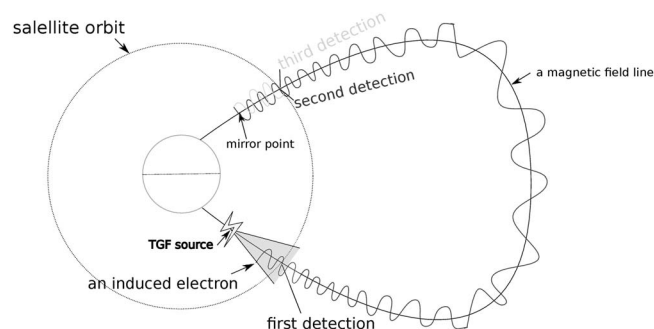


Figure 11. Sketch describing the geometry of an MC-PEPTITA simulation. The TGF source is made only of photons that can produce electrons that may escape and follow the presented trajectory and may be detected three times at satellite altitude. The three detections correspond to the three columns of Figure 10.

3.4. Spatial Distribution of Leptons

In Figure 10 we represent scatterplots of electrons and positrons reaching satellite altitude in both hemispheres, with the three columns corresponding to three detections. The geometry of the simulation is presented in Figure 11. The displayed δ and q distances are relative to the center of the electron or positron beam of a given hemisphere. The calculation of δ and q from geographical coordinates of the particles is explained in section A4.

For this simulation, the electron beam is following an average magnetic field line that intercepts the detection sphere (550 km altitude) in the Southern Hemisphere at -6.91° latitude and 32.4° longitude. At the intersection point, in the Southern Hemisphere and in ECEF coordinates (Figure 1), the magnetic field line has a tangent vector of about (0.58, 0.33, 0.74). The conjugate point in the Northern Hemisphere, at ground level, is located at 32.6° longitude and 29.7° latitude, which is quite close to the values presented in Briggs *et al.* [2011].

In Figure 10, the scatterplots can be enclosed by elliptic shapes. Indeed, the charged particles are roughly confined in a cylinder, within a small altitude interval. At the point where the particles cross the 550 km sphere (in the Southern Hemisphere), the angle between the magnetic field and a plane tangent to the sphere is about $\kappa = 30^\circ$ for the considered geometric configuration. A cylinder intersecting a plane with this relative angle will make an ellipse with an eccentricity of about $e = 0.5$. This effect is similar in the Southern Hemisphere. Ellipses containing 25%, 50%, and 90% of the particles are displayed in Figure 10, together with the value of their equivalent radius. An equivalent radius R_{eq} corresponds to the radius of the beam in a plane perpendicular to the magnetic field line. It can be deduced with $R_{eq} = a \times \cos(\kappa)$, where a is the semimajor axis of the ellipses displayed in Figure 10.

In the Southern Hemisphere, 50% of the electrons are included within $R_{eq} \sim 20$ km radial distance. The radius of this electron beam seems different from Dwyer *et al.* [2008], where most of the electrons and positrons reaching 500 km altitude are confined inside a circle of 10 km radius. We assume that, in this model, electrons are produced above 40 km, most of them within a scale height (of ~ 7 km), leading to beams with ~ 10 km radius. Electrons produced above 50–60 km may be present but are not discussed. In MC-PEPTITA, the interactions of electrons with the atmosphere is nonnegligible until ~ 100 km altitude, and the interactions of photons with the atmosphere has to be considered up to ~ 75 km. In Figure 7, we see that electrons reaching satellite altitude are still produced significantly by photons up to 75 km and by other electrons up to 100 km altitude, as discussed in section 3.2. Nevertheless, the differences between the beam sizes of the two models may be explained partially considering the following points:

1. The simulation presented in Dwyer *et al.* [2008] has a source altitude of 21 km (versus 15 km in this work).
2. Dwyer *et al.* [2008] probably uses initial photons coming from the relativistic feedback theory, which may have a narrower beaming than the one used here (equation (1)).
3. The detection limit is set to 500 km altitude in one case and 550 km in the other.
4. The magnetic field line in Dwyer *et al.* [2008] has a 50° tilt with respect to the detection plane, versus $\sim 30^\circ$ degrees in our case. Since the geomagnetic field models used by both codes are similar, the initial photon source is probably located at a different latitude.

Having larger electron beam radii than previously expected would imply that the TEB/TGF detection ratio of satellites (currently estimated to be about 1/100 [Dwyer *et al.*, 2012]) could be higher. More investigations should be done concerning this point.

Another important information is the bouncing ratio. In this simulation, $\sim 22\%$ of the electrons that reached a first time 550 km altitude in the Northern Hemisphere will bounce on the magnetic mirror point of the Northern Hemisphere: they can cross the detection plane a third time. The bouncing ratio goes down to about 19% for positrons, but the statistics are rather bad. A lower bouncing ratio could be explained considering the pitch angle (the angle between the direction of the particle and the magnetic field). Since they have higher energies, the positrons will be, on average, less deviated than electrons. Thus, the pitch angles of the positrons are, on average, lower than that of electrons; therefore, the altitude of the positron's mirror points may be lower, leading to a lower chance of bouncing.

4. Conclusions

MC-PEPTITA is a Monte Carlo model for the transport of photons, electrons, and positrons with energies above 10 keV. This code takes into account all secondary particles propagating the atmosphere and the geomagnetic field. It includes 11 processes (four for photons, three for electrons, and four for positrons) and uses mainly cross sections from Livermore data (EPDL and EEDL). The interactions are treated in a similar way that is presented in PENELOPE [Salvat *et al.*, 2011]. MC-PEPTITA has been validated by a test case comparison with GEANT4.

By using MC-PEPTITA in a configuration close to a realistic event (Fermi event number 091214), we discussed some features concerning the TGF particles at satellite altitude. The photons arriving at satellite altitude come mainly from the initial source (and may have Compton scattered a few times on the way), but secondary photons, due to Bremsstrahlung and positron annihilation, are important. The main production of secondary electrons reaching satellite altitude is located between 30 and 60 km. The electron beams are confined by the magnetic field, to beams of ~ 20 km radius, because the electrons still interact and can be produced significantly from 50 to 100 km altitude. Finally, the proportion of electrons mirroring at the magnetic conjugate point, given by MC-PEPTITA, is $\sim 22\%$ for this event.

The TARANIS mission [Lefevre *et al.*, 2009], with onboard the X-ray, Gamma-ray and Relativistic Electron experiment (XGRE) and Instrument Détecteurs d'Electrons Energétiques (IDEE) instruments, will have the ability to detect X/gamma rays and electrons from space, including information about the direction of the electrons. Using MC-PEPTITA and GEANT4 to reproduce TARANIS data will help to give constraints on the TGF source mechanism. TARANIS is expected to be launched in spring 2017.

MC-PEPTITA will be used to study other aspects of TGF and induced secondary photons, electrons, and positrons, in particular regarding the temporal distribution of particles that can be seen by a satellite and how it depends on the initial photon source properties. Another important study would be to investigate in which conditions a satellite can detect a positron ratio that can reach 20% or more and how this ratio is dependent on the properties of the initial photon source and on the satellite configuration.

Appendix A: Defining Useful Quantities

A1. Radial Distance

Consider a particle of position (x, y, z) that reached an altitude h_f . If the particles are centered around (λ_s, ϕ_s) , the radial distance d with respect to (λ_s, ϕ_s) and at the altitude h_f can be calculated with

$$d = (R_e + h_f) \arccos(\cos(\varphi)) \quad (A1)$$

$$\mathbf{L} = \begin{pmatrix} \cos(\phi_s) \cos(\lambda_s) \\ \sin(\phi_s) \cos(\lambda_s) \\ \sin(\lambda_s) \end{pmatrix} \quad (A2)$$

$$n = \sqrt{x^2 + y^2 + z^2} \quad (A3)$$

$$\hat{\mathbf{n}} = \frac{1}{n} \begin{pmatrix} x \\ y \\ z \end{pmatrix} \quad (A4)$$

$$\cos(\varphi) = \mathbf{L} \cdot \hat{\mathbf{n}} \quad (A5)$$

A2. Radial Distance Distribution

All the radial distances of the particles are d_n , with $n = 1, \dots, N$ being the particle index, and N the total number of detected particles. The radial distance bins are delimited with the values b_m , with $m = 1, \dots, M$ being the bin index, and M being the total number of bins. This binning is chosen using the Freedman-Diaconis rule [Freedman and Diaconis, 1981] from the d_n data set. The radial distance distribution D_j is then defined for each bin as

$$D_m = \frac{N(d_n \in [b_{m-1}, b_m])}{\pi b_m^2 - \pi b_{m-1}^2} \quad (A6)$$

$N(d_i \in [b_{i-1}, b_i])$ being the number of particles with radial distances between b_{i-1} and b_i . ($\pi b_m^2 - \pi b_{m-1}^2$) is the surface of the halo delimited by radial distances b_{m-1} and b_m .

A3. Energy Spectrum Distribution

For the energies, the bin delimitation ϵ_k can be defined as well using the Freedman-Diaconis rule, $k = 1, \dots, K$ being the bin index and K being the total number of energy bins. The energy spectrum distribution is then defined as

$$P_k = \frac{N(e_k \in [\epsilon_{k-1}, \epsilon_k])}{\epsilon_k - \epsilon_{k-1}} \quad (A7)$$

where e_n corresponds to all the energies of the particles reaching satellite altitude; n is the same as above. $N(e_i \in [\epsilon_{i-1}, \epsilon_i])$ is the number of particles with energies between ϵ_{i-1} and ϵ_i .

A4. q and δ Distances

The q and δ distances are calculated from the longitudes (ϕ_i) and latitudes (λ_i) of the particles crossing the 550 km altitude sphere. It represents the distances following the lines of constant longitude or constant latitude. The calculation is done with

$$q_i = \lambda_i \times (R_E + 550 \text{ km}) \quad (A8)$$

$$\delta_i = \phi_i \times \cos(\lambda_i) \times (R_E + 550 \text{ km}) \quad (A9)$$

where λ_i and ϕ_i are expressed in radians, and R_E is the radius of the Earth. Note that $q_i = 0$ at the equator and $\delta_i = 0$ at Greenwich meridian.

Acknowledgments

We would like to thank the CNES (Centre National d'Etudes Spatiales), the DGA (Direction Generale de l'Armement) for their financial support. We also want to thank the two anonymous reviewers for their recommendations and comments that helped to greatly improve this work. This work was granted access to the HPC resources of CALMIP supercomputing center under the allocation 2015-p1505. The data generated by the GEANT4 or MC-PEPTITA simulations presented in this work can be requested by emailing the corresponding author: david.sarria@irap.omp.eu.

Michael Balikhin thanks the reviewers for their assistance in evaluating this paper.

References

- Agostinelli, S., et al. (2003), GEANT4: A simulation toolkit, *Nucl. Instrum. Methods*, A506, 250–303, doi:10.1016/S0168-9002(03)01368-8.
- Babich, L. P., E. N. Donskoy, I. M. Kutsyk, A. Y. Kudryavtsev, R. A. Roussel-Dupre, B. N. Shamarov, and E. M. D. Symbalisty (2001), Comparison of relativistic runaway electron avalanche rates obtained from Monte Carlo simulations and kinetic equation solution, *IEEE Trans. Plasma Sci.*, 29, 430–438, doi:10.1109/27.928940.
- Briggs, M. S., et al. (2010), First results on terrestrial gamma ray flashes from the Fermi Gamma-ray Burst Monitor, *J. Geophys. Res.*, 115, A07323, doi:10.1029/2009JA015242.
- Briggs, M. S., et al. (2011), Electron-positron beams from terrestrial lightning observed with Fermi GBM, *Geophys. Res. Lett.*, 38, L02808, doi:10.1029/2010GL046259.
- Briggs, M. S., et al. (2013), Terrestrial gamma-ray flashes in the Fermi era: Improved observations and analysis methods, *J. Geophys. Res. Space Physics*, 118, 3805–3830, doi:10.1002/jgra.50205.
- Carlson, B. E., N. G. Lehtinen, and U. S. Inan (2007), Constraints on terrestrial gamma ray flash production from satellite observation, *Geophys. Res. Lett.*, 34, L08809, doi:10.1029/2006GL029229.
- Carlson, B. E., N. G. Lehtinen, and U. S. Inan (2008), Runaway relativistic electron avalanche seeding in the Earth's atmosphere, *J. Geophys. Res.*, 113, A10307, doi:10.1029/2008JA013210.
- Carlson, B. E., N. G. Lehtinen, and U. S. Inan (2009), Observations of terrestrial gamma-ray flash electrons, in *Coupling of Thunderstorms and Lightning Discharges to Near-Earth Space: Proceedings of the Workshop, AIP Conf. Proc.*, vol. 1118, edited by N. B. Crosby, T. -Y. Huang, and M. J. Rycroft, pp. 84–91, Am. Inst. of Phys., Melville, New York, doi:10.1063/1.3137717.
- Carlson, B. E., N. G. Lehtinen, and U. S. Inan (2010), Terrestrial gamma ray flash production by active lightning leader channels, *J. Geophys. Res.*, 115, A10324, doi:10.1029/2010JA015647.
- Carlson, B. E., T. Gjesteland, and N. Østgaard (2011), Terrestrial gamma-ray flash electron beam geometry, fluence, and detection frequency, *J. Geophys. Res.*, 116, A11217, doi:10.1029/2011JA016812.
- Celestin, S., W. Xu, and V. P. Pasko (2012), Terrestrial gamma ray flashes with energies up to 100 MeV produced by nonequilibrium acceleration of electrons in lightning, *J. Geophys. Res.*, 117, A05315, doi:10.1029/2012JA017535.
- Coleman, L. M., and J. R. Dwyer (2006), Propagation speed of runaway electron avalanches, *Geophys. Res. Lett.*, 33, L11810, doi:10.1029/2006GL025863.
- Cullen, D. E., J. H. Hubbell, and L. Kissel (1997), Epd197: The evaluated photon data library, '97 version, UCRL-50400, Vol. 6, Rev. 5, 19 Sept. 1997, Lawrence Livermore Natl. Lab.
- Cummer, S. A., M. S. Briggs, J. R. Dwyer, S. Xiong, V. Connaughton, G. J. Fishman, G. Lu, F. Lyu, and R. Solanki (2014), The source altitude, electric current, and intrinsic brightness of terrestrial gamma ray flashes, *Geophys. Res. Lett.*, 41, 8586–8593, doi:10.1002/2014GL02196.
- Dwyer, J. R. (2007), Relativistic breakdown in planetary atmospheres, *Phys. Plasmas*, 14(4), 042901, doi:10.1063/1.2709652.
- Dwyer, J. R. (2008), Source mechanisms of terrestrial gamma-ray flashes, *J. Geophys. Res.*, 113, D10103, doi:10.1029/2007JD009248.
- Dwyer, J. R. (2012), The relativistic feedback discharge model of terrestrial gamma ray flashes, *J. Geophys. Res.*, 117, A02308, doi:10.1029/2011JA017160.
- Dwyer, J. R., and D. M. Smith (2005), A comparison between Monte Carlo simulations of runaway breakdown and terrestrial gamma-ray flash observations, *Geophys. Res. Lett.*, 32, L22804, doi:10.1029/2005GL023848.
- Dwyer, J. R., B. W. Grefenstette, and D. M. Smith (2008), High-energy electron beams launched into space by thunderstorms, *Geophys. Res. Lett.*, 35, L02815, doi:10.1029/2007GL032430.

- Dwyer, J. R., D. M. Smith, and S. A. Cummer (2012), High-energy atmospheric physics: Terrestrial gamma-ray flashes and related phenomena, *Space Sci. Rev.*, **173**, 133–196, doi:10.1007/s11214-012-9894-0.
- Finlay, C. C., et al. (2010), International geomagnetic reference field: The eleventh generation, *Geophys. J. Int.*, **183**, 1216–1230, doi:10.1111/j.1365-246X.2010.04804.x.
- Fishman, G. J., et al. (1994), Discovery of intense gamma-ray flashes of atmospheric origin, *Science*, **264**, 1313–1316, doi:10.1126/science.264.5163.1313.
- Freedman, D., and P. Diaconis (1981), On the histogram as a density estimator: L2 theory, *Z. Wahrscheinlichkeit.*, **57** (4), 453–476, doi:10.1007/BF01025868.
- Gjesteland, T., N. Østgaard, A. B. Collier, B. E. Carlson, M. B. Cohen, and N. G. Lehtinen (2011), Confining the angular distribution of terrestrial gamma ray flash emission, *J. Geophys. Res.*, **116**, A11313, doi:10.1029/2011JA016716.
- Gurevich, A. V., G. M. Milikh, and R. Roussel-Dupre (1992), Runaway electron mechanism of air breakdown and preconditioning during a thunderstorm, *Phys. Lett. A*, **165**, 463–468, doi:10.1016/0375-9601(92)90348-P.
- Hazeltin, B. J., B. W. Grefenstette, D. M. Smith, J. R. Dwyer, X.-M. Shao, S. A. Cummer, T. Chronis, E. H. Lay, and R. H. Holzworth (2009), Spectral dependence of terrestrial gamma-ray flashes on source distance, *Geophys. Res. Lett.*, **36**, L01108, doi:10.1029/2008GL035906.
- Kalos, M. H. (1986), *Monte Carlo Methods. Vol. 1: Basics*, Wiley, New York.
- Lefevre, F., E. Blanc, and J. L. Pinçon (2009), TARANIS-A satellite project dedicated to the physics of TLEs and TGFs, in *Coupling Of Thunderstorms and Lightning Discharges to Near-Earth Space: Proceedings of the Workshop. AIP Conf. Proc.*, vol. 1118, edited by N. B. Crosby, T.-Y. Huang, and M. J. Rycroft, pp. 84–91, Am. Inst. of Phys., Melville, New York, doi:10.1063/1.3137711.
- Liu, N., and J. R. Dwyer (2013), Modeling terrestrial gamma ray flashes produced by relativistic feedback discharges, *J. Geophys. Res. Space Physics*, **118**, 2359–2376, doi:10.1002/jgra.50232.
- Marisaldi, M., et al. (2010), Detection of terrestrial gamma ray flashes up to 40 MeV by the AGILE satellite, *J. Geophys. Res.*, **115**, A00E13, doi:10.1029/2009JA014502.
- Marisaldi, M., et al. (2011), AGILE observations of terrestrial gamma-ray flashes, ArXiv e-prints.
- Neubert, T., and ASIM Instrument Team (2009), ASIM—an Instrument Suite for the International Space Station, *AIP Conference Proceedings*, **1118**(1), 8–12, doi:10.1063/1.3137718.
- Østgaard, N., T. Gjesteland, J. Stadsnes, P. H. Connell, and B. Carlson (2008), Production altitude and time delays of the terrestrial gamma flashes: Revisiting the burst and transient source experiment spectra, *J. Geophys. Res.*, **113**, A02307, doi:10.1029/2007JA012618.
- Perkins, S. T., D. E. Cullen, and S. M. Seltzer (1991), Tables and graphs of electron-interaction cross sections from 10 eV to 100 GeV derived from the LLNL Evaluated Electron Data Library (EEDL), Z = 1 to 100, *Tech. Rep.*, Lawrence Livermore Natl. Lab., Calif.
- Picone, J. M., A. E. Hedin, D. P. Drob, and A. C. Aikin (2002), NRLMSISE-00 empirical model of the atmosphere: Statistical comparisons and scientific issues, *J. Geophys. Res.*, **107**(A12), 1468, doi:10.1029/2002JA009430.
- Salvat, F., A. Jablonski, and C. J. Powell (2005), Elsepa–Dirac partial-wave calculation of elastic scattering of electrons and positrons by atoms, positive ions and molecules, *Comput. Phys. Commun.*, **165**(2), 157–190, doi:10.1016/j.cpc.2004.09.006.
- Salvat, F., J. M. Fernández-Varea, and J. Sempau (2011), *PENELOPE-2011: A Code System for Monte Carlo Simulation of Electron and Photon Transport*, OECD Nucl. Energy Agency, Issy-les-Moulineaux, France.
- Seltzer, S. M., and M. J. Berger (1986), Bremsstrahlung energy spectra from electrons with kinetic energy 1 keV–10 GeV incident on screened nuclei and orbital electrons of neutral atoms with Z = 1–100, *At. Data Nucl. Data Tables*, **35**, 345, doi:10.1016/0092-640X(86)90014-8.
- Skelved, A. B., N. Østgaard, B. Carlson, T. Gjesteland, and S. Celestin (2014), Modeling the relativistic runaway electron avalanche and the feedback mechanism with geant4, *J. Geophys. Res. Space Physics*, **119**, 9174–9191, doi:10.1002/2014JA020504.
- Smith, D. M., L. I. Lopez, R. P. Lin, and C. P. Barrington-Leigh (2005), Terrestrial gamma-ray flashes observed up to 20 MeV, *Science*, **307**, 1085–1088, doi:10.1126/science.1107466.
- Smith, D. M., et al. (2006), The anomalous terrestrial gamma-ray flash of 17 January 2004, *Eos Trans. AGU*, **87**(52), Fall Meet. Suppl., Abstract AE31A-1040.
- Smith, D. M., et al. (2011), The rarity of terrestrial gamma-ray flashes, *Geophys. Res. Lett.*, **38**, L08807, doi:10.1029/2011GL046875.
- Surkov, V. V., and M. Hayakawa (2012), Underlying mechanisms of transient luminous events: A review, *Ann. Geophys.*, **30**, 1185–1212, doi:10.5194/angeo-30-1185-2012.
- Williams, E., et al. (2006), Lightning flashes conducive to the production and escape of gamma radiation to space, *J. Geophys. Res.*, **111**, D16209, doi:10.1029/2005JD006447.
- Williams, E. R. (2010), Origin and context of C. T. R. Wilson's ideas on electron runaway in thunderclouds, *J. Geophys. Res.*, **115**, A00E50, doi:10.1029/2009JA014581.